12 (2022) 100256

Contents lists available at ScienceDirect

Biosensors and Bioelectronics: X

journal homepage: www.journals.elsevier.com/biosensors-and-bioelectronics-x

Label-free electrochemical aptasensor for the detection of SARS-CoV-2 spike protein based on carbon cloth sputtered gold nanoparticles

Muhammad Adeel [a,b,c,*], Kanwal Asif [a,b], Fahad Alshabouna [c,d], Vincenzo Canzonieri [b,e], Md. Mahbubur Rahman [f], Sajid Ali Ansari [g], Firat Güder [c], Flavio Rizzolio [a,b], Salvatore Daniele [a,**]

[a] Department of Molecular Sciences and Nanosystems, Ca'Foscari University of Venice, 30123, Venezia, Italy
[b] Pathology Unit, Centro di Riferimento Oncologico di Aviano (CRO) IRCCS, 33081, Aviano, Italy
[c] Department of Bioengineering, Imperial College London, London, SW7 2AZ, UK
[d] Center of Excellence for Advanced Materials and Manufacturing, King Abdulaziz City for Science and Technology, 11442, Riyadh, Saudi Arabia
[e] Department of Medical, Surgical and Health Sciences, University of Trieste, 34127, Trieste, Italy
[f] Department of Applied Chemistry, Konkuk University, Chungju, 27478, South Korea
[g] Department of Physics, College of Science, King Faisal University, P. O. Box 400, Hofuf, Al-Ahsa, 31982, Saudi Arabia

ARTICLE INFO

Keywords:
Flexible carbon cloth
Aptamers
Electrochemical sensing
COVID-19
Spike protein
Diagnostics

ABSTRACT

The proliferation and transmission of the severe acute respiratory syndrome coronavirus 2 (SARS-CoV-2), or the (COVID-19) disease, has become a threat to worldwide biosecurity. Therefore, early diagnosis of COVID-19 is crucial to combat the ongoing infection spread. In this study we propose a flexible aptamer-based electrochemical sensor for the rapid, label-free detection of SARS-CoV-2 spike protein (SP). A platform made of a porous and flexible carbon cloth, coated with gold nanoparticles, to increase the conductivity and electrochemical performance of the material, was assembled with a thiol functionalized DNA aptamer *via* S–Au bonds, for the selective recognition of the SARS-CoV-2 SP. The various steps for the sensor preparation were followed by using scanning electron microscopy, cyclic voltammetry and differential pulse voltammetry (DPV). The proposed platform displayed good mechanical stability, revealing negligible changes on voltammetric responses to bending at various angles. Quantification of SARS-CoV-2 SP was performed by DPV and chronopotentiometry (CP), exploiting the changes of the electrical signals due the $[Fe(CN)_6]^{3-/4-}$ redox probe, when SARS-CoV-2 SP binds to the aptamer immobilized on the electrode surface. Current density, in DPV, and square root of the transition time, in CP, varied linearly with the log[SARS-CoV-2 SP], providing lower limits of detection (LOD) of 0.11 ng/mL and 37.8 ng/mL, respectively. The sensor displayed good selectivity, repeatability, and was tested in diluted human saliva, spiked with different SARS-CoV-2 SP concentrations, providing LODs of 0.167 ng/mL and 46.2 ng/mL for DPV and CP, respectively.

1. Introduction

The severe acute respiratory syndrome coronavirus 2 (SARS-CoV-2), or the coronavirus disease-19 (COVID-19), outbreak, first reported in December 2019 (El Keshky et al., 2020; Wang et al., 2020), is causing colossal dysfunction of various activities that challenge global human health and economy. The virus spreads via respiratory droplets, including aerosols, from an infected, mostly asymptomatic, person who breathes in close proximity to other people (Adeel et al., 2022; Lukose et al., 2021; Raziq et al., 2021; Zhao et al., 2021). Recently, launched vaccines against COVID-19 have failed to prevent the spread (Wouters et al., 2021). Therefore, early detection of the disease is as crucial now as during the onset of the pandemic.

Reverse transcription polymerase chain reaction (RT-PCR) is considered the gold standard COVID-19 diagnostic technique (Adeel et al., 2022; Da Ruos et al., 2022; Rahman, 2022). However, it requires trained personnel and laboratory setup, is slow and costly. Lateral flow assays (LFAs), which use colorimetric measurements, are an alternative

* Corresponding author.
** Corresponding author. Department of Molecular Sciences and Nanosystems, Ca'Foscari University of Venice, 30123, Venezia, Italy.
E-mail addresses: m.adeel@imperial.ac.uk (M. Adeel), sig@unive.it (S. Daniele).

https://doi.org/10.1016/j.biosx.2022.100256
Received 16 July 2022; Received in revised form 5 September 2022; Accepted 17 September 2022
Available online 24 September 2022

to RT-PCR to detect COVID-19. They provide a solution to the above-mentioned issues, yet the accuracy of these methods remains an unsolved problem. Furthermore, LFAs are difficult to digitize, thus hindering their practical application in traceability systems. For these reasons, antigen tests have been authorized by FDA to detect SARS-CoV-2 in emergency use situations ("Coronavirus Disease 2019 (COVID-19) Emergency Use Authorizations for Medical Devices, FDA," 2020). Other methods available for the detection of SARS-CoV-2 include immunological and serological tests, which detect the antibodies developed upon exposure to the virus (Hachim et al., 2020; Kevadiya et al., 2021; Lai et al., 2021; Taleghani and Taghipour, 2021; Yüce et al., 2021). These tests are more reliable for the detection of SARS-CoV-2; however, apart from requiring a laboratory setup, they are not suitable at early-stage infection because detectable levels of antibodies are developed 10–14 days after the onset of the symptoms (Raziq et al., 2021; Ying et al., 2020). There is therefore an utmost need for simple, accurate, rapid, and sensitive diagnostic methods for the detection of SARS-CoV-2 antigens, through portable devices, which do not require trained personnel.

For early-stage detection of COVID-19, spectroscopic and electrochemical biosensors have been developed (Lim and Ahmed, 2016; Seo et al., 2020; Stanborough et al., 2021; Rahman, 2022), typically targeting the SARS-CoV-2 spike protein (SP), which is one of the four major structural proteins of SARS-CoV-2 expressed on the surface of the viral particles (Lim and Ahmed, 2016). Electrochemical devices have a number of advantages in biosensing, including: point-of-care and point-of-need testing, rapid measurements, high degree of automation at low power consumptions, and shorter assay times (Adeel et al., 2021a, 2021b, 2020; Jiang et al., 2022; Kumar et al., 2022; Lim and Ahmed, 2016). Recently, several articles have reported on the detection of SARS-CoV-2 SP using electrochemical biosensors based on antibodies as recognition elements (Adeel et al., 2022; Beduk et al., 2021; Chaibun et al., 2021; Jiang et al., 2022; Kumar et al., 2022; Yakoh et al., 2021). These devices, in general, offer great possibility for the label-free detection of target analytes by exploiting even small changes of electrochemical signals (i.e., current, potential, etc.) due to a variety of redox probes (e.g., $[Fe(CN)_6]^{3-/4-}$, $[Ru(NH_3)_6]^{3+}$ etc.). However, the antibody-based biosensors suffer from several limitations, including poor stability and high cost of the antibodies, and the need for complex chemical modifications to make them suitable for detecting the target analyte (Adeel et al., 2019; Lopa et al., 2019). To overcome these limitations, aptamers (short strands of oligonucleotide) could also be employed as biorecognition elements. In fact, similar to the antibody, they are selective for the target analytes (Jo et al., 2015; Maehashi et al., 2007; Medley et al., 2008; Min et al., 2008), can be easily functionalized (Min et al., 2008), and form three-dimensional unique binding sites against their targets (Lim and Ahmed, 2016).

For the fabrication of electrochemical biosensors, screen-printed or classical disk-shaped glassy carbon electrodes have often been used as substrates. They are then modified with a variety of nanomaterials to enhance both sensitivity and selectivity in the measurements (Adeel et al., 2020, 2021b; Bai et al., 2019; Cho et al., 2020; Hopkins et al., 2019; Khan, 2021; Kour et al., 2020; Lu et al., 2021; Maduraiveeran and Jin, 2017; Pirzada and Altintas, 2019; Zhang et al., 2015). However, the surface modification, in some cases, introduces other drawbacks, such as low conductivity and biocompatibility of the coating materials, or require complex procedures to introduce suitable functional groups on their surfaces (Adeel et al., 2020, 2021a). Therefore, there is an utmost need to construct electrode platforms using simple electrode modification procedures, adopting a single biocompatible material. These aspects are relevant in the contest of the war against COVID-19, for which it is quite beneficial to develop novel strategies in constructing low cost and highly sensitive devices for the detection of the SARS-CoV-2 SP.

In this work, we propose a low-cost aptamer-based electrochemical sensor (apta-sensor) for the detection of SARS-CoV-2 SP, using a flexible carbon cloth (CC), as primary substrate, which is modified with gold nanoparticles (AuNPs). The AuNPs allow the immobilization on the substrate surface of a thiol functionalized DNA aptamer *via* S–Au bonds, thus providing a stable platform enabling the binding SARS-CoV-2 SP to the aptamer and its detection, by exploiting the change of electrochemical responses that arise from the $[Fe(CN)_6]^{3-/4-}$ redox couple (Fig. 1). Differential pulse voltammetry (DPV) and chronopotentiometry (CP) are employed as electrochemical techniques for quantification, the latter rarely employed for biosensing purposes. The sensor proposed here is used to quantify the SARS-CoV-2 SP in phosphate-buffer saline (PBS) and diluted human saliva.

2. Experimental

2.1. Materials and reagents

Bovine serum albumins (≥98%, BSA), human serum albumins (≥98%, HSA), potassium hexacyanoferrate (II) (≥99%, $K_4[Fe(CN)_6]$) and potassium hexacyanoferrate (III) (≥99%, $K_3[Fe(CN)_6]$), were purchased from Sigma Aldrich (St. Louis, MO, USA). Dulbecco's phosphate-buffer saline (PBS), pH 7.4, without calcium and magnesium chloride, was purchased from Thermo Fisher Scientific (Waltham, Massachusetts, USA). Artificial human saliva for research purposes was purchased from LCTech (Germany). Flexible CC (Sigracet 39 BB, SGL Carbon) was purchased from Fuel Cell store (Germany). Thiol functionalized SARS-CoV-2 spike S1 aptamer (apta-SARS-CoV-2 (seq.name CFA0688T-GQ5-100, 5′- ThiolC6 – aptamer-3′), SARS-CoV-2 SP, and SARS-CoV SP were purchased from Cambio Ltd. (UK). Ultrapure water (resistivity 18 MΩ) was prepared by a Milli-Q® IX water purification system (Sigma Aldrich). Pure nitrogen (N_2, >99.99%) was supplied from SIAD (Bergamo, Italy).

2.2. Apparatus

The Field-emission scanning electron microscope (FE-SEM, Carl Zeiss Sigma VP) was used to examine the morphology of the electrodes. Energy-dispersive X-ray spectroscopy (EDS) (Quantax 200) associated with the FE-SEM were employed for elemental analyses. A plasma sputter-coater (mini deposition system) Balzers Med 010 (Austin, TX, USA) was employed for the deposition of AuNPs on the CC surfaces.

A CHI920C workstation (CH Instruments, TX, USA) was utilized for voltammetric and chronopotentiometric measurements. These were performed in an electrochemical cell in the three-electrode configuration using the modified/unmodified CC as the working electrodes, a Pt wire and an Ag/AgCl (KCl, saturated) as counter and reference electrode, respectively. The surface area of the working electrodes was 0.196 cm^2, as defined by the O-ring of a homemade holder (Fig. S1). DPVs were acquired by using the following optimized parameters: pulse width 2 ms, pulse amplitude 100 mV, pulse period 1 s. Unless otherwise stated, for the electrochemical characterization of the electrode materials and the SARS-CoV-2 SP quantification, the measurements were performed in a PBS (pH 7.4) solution containing $[Fe(CN)_6]^{3-/4-}$ (3 mM each) as redox probe.

2.3. Modification of the carbon cloth with AuNPs

A series of CC (each 2×4 cm^2) was cleaned using deionized water by sonication (10 min) and then dried with a stream of pure N_2. AuNPs were sputtered on the CC surface using a plasma sputter-coater under the following conditions: current 40 mA; sputtering time of 10, 20 and 30 s; working pressure of 0.05 mbar; in all cases the coating procedure was performed under an argon atmosphere. As will discussed later, only the 30 s gold coated CC was used to prepare the apta-sensor system.

2.4. Fabrication of the apta-sensor

The scheme of the preparation of the apta-sensor is shown in Fig. 1.

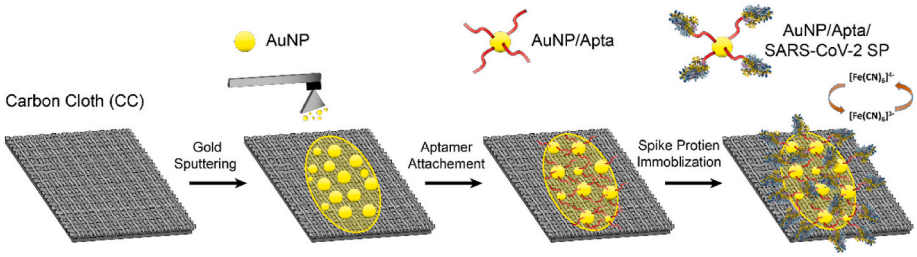

Fig. 1. Schematic illustration of the SARS-CoV-2 SP apta-sensor preparation. It includes the following steps: AuNPs coating on carbon cloth (CC); immobilization of thiol functionalized SARS-CoV-2 aptamer on AuNPs surface (apta/AuNPs/CC); binding of SARS-CoV-2 SP at the apta/AuNPs/CC; label-free detection of SARS-CoV-2 SP using the $[Fe(CN)_6]^{3-/4-}$ redox couple.

The thiol functionalized apta-SARS-CoV-2 was covalently attached on the surface of the 30 s AuNPs/CC *via* S–Au bond. Briefly, the AuNPs/CC was placed in the electrochemical cell (i.e., the holder with the confined geometric area defined by the O-ring). 400 μL of the aptamer solution (1 μg/mL in PBS pH 7.4, prepared according to the manufacturer's instructions) was dropped on the AuNPs/CC surface and incubated at 4 °C for 6 h. Thereafter, the aptamer modified AuNPs/CC (apta/AuNPs/CC) was washed with PBS to remove the physically adsorbed aptamer. Subsequently, 1% BSA solution (400 μL, prepared in Milli-Q water) was dropped onto the apta/AuNPs/CC platform and kept for 1 h at 4 °C to block the unspecific binding sites of the apta-sensor. The apta/AuNPs/CC thus prepared was used to bind SARS-CoV-2 SP at different concentrations. After each addition of SARS-CoV-2 SP, the system was allowed to equilibrate for 30 min at 4 °C and washed with PBS (pH 7.4) prior to the electrochemical measurements.

3. Results and discussions

3.1. Surface analysis of the CC and AuNPs/CC electrodes

Fig. 2a, d shows the FE-SEM images of the bare CC, and the 10 s, 20 s and 30 s coated CC electrodes (AuNPs/CC). As is evident, the bare CC surface exhibits small wrinkles, while the various AuNPs/CCs show that the surface is coated with AuNPs of size less than 100 nm. By increasing only the sputtering time, however, the AuNPs density increases thus covering more surface of the CC (exposed to the sputtering target) (Fig. 2c and d), while the sizes of the particles remain essentially the same. The 30 s AuNPs/CC exhibits a rather high porous architecture and an almost complete CC surface coverage with AuNPs. This was further confirmed by EDS elemental mapping (Fig. 2e), as well as by the EDS elemental spectra Fig. 2f. For comparison, the EDS spectrum of the bare

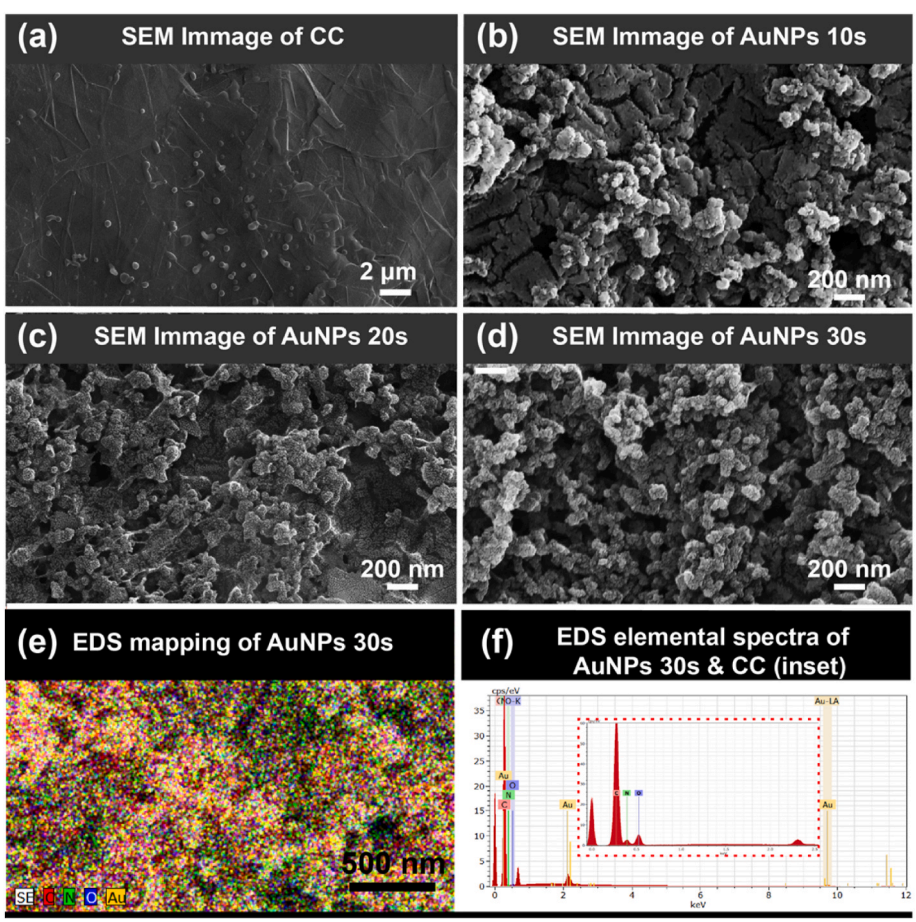

Fig. 2. FE-SEM images of (a) bare CC, (b) 10 s AuNPs-coated CC, (c) 20 s AuNPs-coated CC, (d) 30 s AuNPs-coated CC, (e) EDS mapping obtained at the 30 s AuNPs-coated CC, (f) EDS elemental spectra of for the 30s AuNPs-coated CC and bare CC (inset).

CC is also shown in the inset of Fig. 2f. The elements O, N, C found in the bare CC are also evident in the AuNPs/C. The intense Au peak appeared only after gold sputtering, thus indicating the successful deposition of AuNPs on the bare CC surface (Fig. 2f).

3.2. Electrochemical behavior of the CC and Au/CC electrodes

The electrochemical behavior of the bare CC and of the various AuNPs/CC substrates was characterized by cyclic voltammetry (CV) and differential pulse voltammetry (DPV), using the redox couple $[Fe(CN)_6]^{3-/4-}$ in a phosphate buffer (PBS, pH 7.4) solution. A rather broad and scarcely defined couple of peaks, with peak-to-peak separation (ΔE_p) of 0.276 V and relatively low current intensities were recorded by CV at the bare CC (Fig. S2a). This denoted a relatively slow heterogeneous electron transfer process. The CV responses were improved after the Au sputtering in terms of both ΔE_p and current density to an extent that depended on the amount of AuNPs deposited on the CC surface (Figs. S2c and e and Fig. 3a). In particular, ΔE_p decreased to 0.152 V, 0.120 V, and 0.088 V for the 10 s, 20 s and 30 s AuNPs/CC substrates, respectively, indicating the substantial enhancement of the electron transfer process, passing from the bare CC to the 30 s AuNPs/CC electrode. The anodic peak current density (J_{pa}) also increased from about 450 μA cm^{-2} for the CC to about 2200 μA cm^{-2} for the 30 s AuNPs/CC, denoting a higher surface area due to the increased porous structure of the AuNPs/CC substrates. DPV measurements confirmed the improvement of the current signal, upon coating the CC with AuNPs (Figs. S2a,d, f and Fig. 3a and b). In fact, J_{pa} values of 104.3 μA/cm^2, 853.5 μA/cm^2, 1750.1 μA/cm^2, and 2464.3 μA/cm^2 were recorded at the bare CC and the 10 s, 20 s and 30 s AuNPs/CC substrates, respectively. The voltametric responses were reproducible (within 1% RSD, obtained from three replicates of peak current density) as verified by repetitive measurement performed with the same substrates (Figs. S2b–f and Fig. 3a–b). The changes observed in the voltammetric responses, due to the AuNPs coating the CC substrate, are compared in Fig. S3. From these results, it is evident that the best performances, especially in terms of current densities, by both CV and DPV, are obtained at the 30 s AuNPs/CC electrode. Therefore, in what follows, only the latter electrode is considered further, as its general characteristics are adequate for an electrochemical platform (*vide infra*).

The 30 s AuNPs/CC electrode was further characterized by CV in the

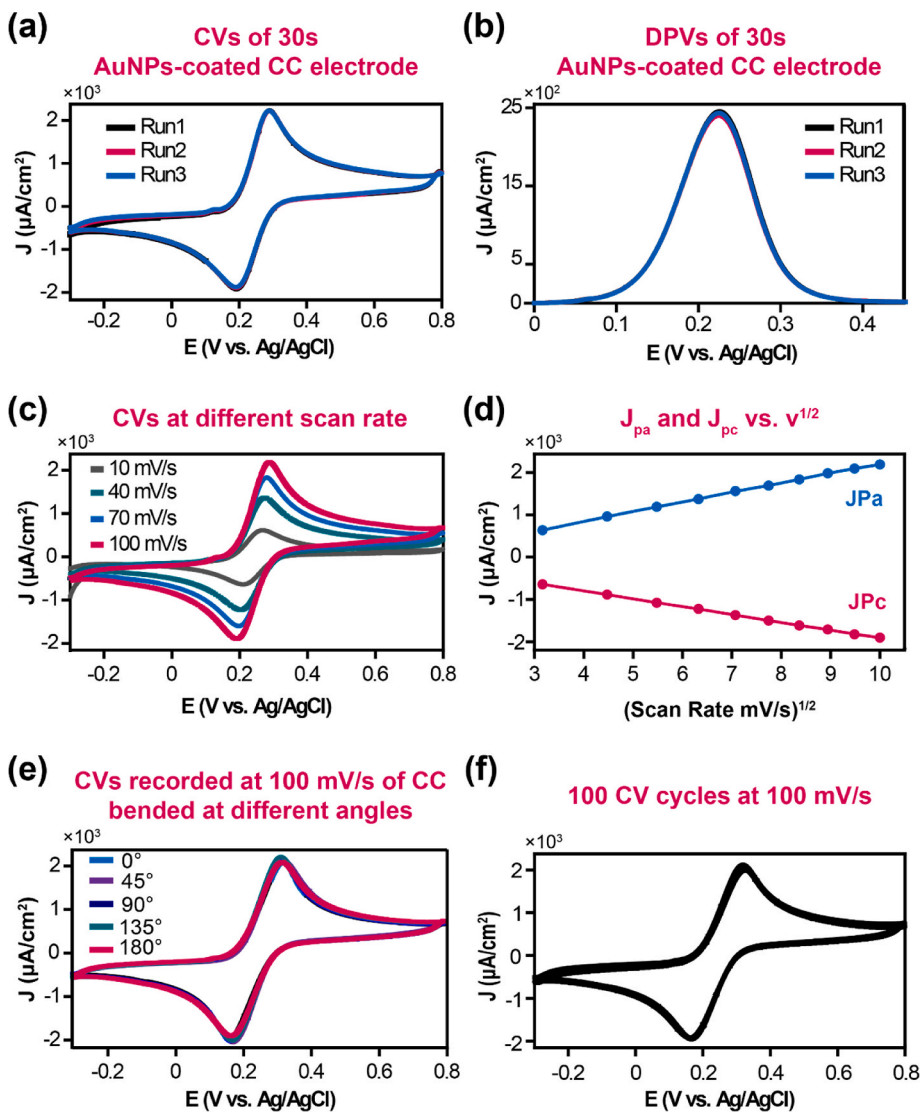

Fig. 3. (a–b) series of CVs and DPVs obtained at the 30 s AuNPs/CC electrode; (c) CVs performed at different scan rates (i.e., 10, 20, 30, 40, 50, 60, 70, 80, 90 and 100 mV/s; (d) plots of J_{pa} and J_{pc} vs. $v^{1/2}$, obtained from the CVs in (c); (e) CVs recorded at 100 mV/s at the 30 s AuNPs/CC bended at different angles (0°, 45°, 90°, 135°, 180°); (f) 100 CV cycles recorded at 100 mV/s at the 30 s AuNPs/CC. All measurements were performed in the solution containing the $[Fe(CN)_6]^{3-/4-}$ redox probe.

presence of the $[Fe(CN)_6]^{3-/4-}$ redox probe to ascertain the mass transport characteristics that apply to the electrode surface and whether bending the substrate, which is flexible, could affect the voltammetric responses. Fig. 3c shows a series of CVs obtained in the $[Fe(CN)_6]^{3-/4-}$ solution at different scan rates over the range 10–100 mV/s. Both J_{pa} and cathodic peak current density (J_{pc}) were linear as a function of the square root of the scan rate ($v^{1/2}$) (Fig. 3d), indicating the occurrence of a diffusion-controlled process (Bard and Faulkner, 2001). To investigate the effect of the mechanical properties of the substrate, the 30 s AuNPs/CC electrode was subjected to repeated bending cycles at different angles (i.e., 0°, 45°, 90°, 135° and 180°), afterward CVs were run at 100 mV/s. The bending stability was assessed based on the hypothesis that eventual structural fracture would create cracks or defects on the surface of the AuNPs/CC and consequently would change the appearance of the surface area of the electrodes, which would reflect on the CV responses. As is shown in Fig. 3e, the CV responses remained essentially unchanged, regardless of the bending angles to which the AuNPs/CC electrode was subjected, this denoting a high stability of the substrate electrode. Furthermore, the stability of the AuNPs/CC electrode was also examined by continuously running CVs cycles at 100 mV/s. As can be seen from Fig. 3f, stable CVs were recorded even after 100 cycles; the J_{pa} analysis provided an RSD of 2.13%.

The electrochemical behavior of the 30 s AuNPs/CC and, for comparison, that of the bare CC was also investigated by chronopotentiometry, using the $[Fe(CN)_6]^{3-/4-}$ redox couple. This technique involves the measurement of the electrode potential during an electrode process occurring at constant current (Bard and Faulkner, 2001). At some moment (called the transition time), the analyte concentration at the electrode surface drops to zero causing an abrupt change of the electrode potential. Consequently, the transition time (τ) can be used to obtain information about the nature and concentration of the species involved in the redox process. In particular, for quantification purposes, the parameter $\tau^{1/2}$ can be used, as it varies linearly with the analyte concentration, as predicted by the Sand equation (**Equation S1**) (Bard and Faulkner, 2001). Here, CP with current reversal (Bard and Faulkner, 2001) was employed using the same anodic and cathodic current values. The potential limits were prefixed at 0.5 V and 0.0 V, where at the AuNPs/CC, the oxidation of $[Fe(CN)_6]^{4-}$ and the reduction of $[Fe(CN)_6]^{3-}$ processes, respectively, occurred under diffusion control. Fig. S4a shows typical chronopotentiograms recorded using 0.512, 1.53 and 3.06 mA cm^{-2}. The forward current is positive, therefore, the potential, from almost the half wave potential of the $[Fe(CN)_6]^{3-/4-}$ systems (as observed from the CV in Fig. S4a) moves towards more positive values up to 0.5 V; the negative backward current leads to the decrease of the potential down to 0 V. From the series of measurements, performed under the above different current density values, the most suitable current density to be applied to the electrode was considered 0.512 mA cm^{-2}. In addition, for quantification purposes, the reversal current stage was employed, as it appeared more reproducible. In fact, a series of five measurements, provided τ values that were reproducible within 0.8% RSD (Fig. S4b). For the reversal current step, a linear relationship also exists between $\tau^{1/2}$ and redox probe concentration (Bard and Faulkner, 2001).

3.3. Optimization of the apta-sensor

The apta-SARS-CoV-2 was immobilized onto the 30 s AuNPs/CC electrode, *via* S–Au covalent bonding (Adeel et al., 2019), in a 400 μL PBS solution containing 1 μg/mL of aptamer, using incubation times of 1 h, 3 h, 5 h, 12 h and 24 h. The concentration of the aptamer employed was considered adequate, since the SARS-CoV-2 SP to be detected is around tens of ng/mL. The success of the aptamer immobilizing strategy and the time needed to achieve a stable layer on the AuNPs/CC electrode were followed by DPV using the $[Fe(CN)_6]^{3-/4}$ redox probe. The key concept of this choice is that the attachment of the apta-SARS-CoV-2 partially passivates the electrode surface and the heterogeneous electron transfer process of the redox probe is somewhat inhibited (Amatore et al., 1983). As is shown in Figs. S5(a and b), the current decreases with time up to 5 h, indicating the completeness of the aptamer attachment *via* S–Au bonds. Therefore, 5 h was used, as the optimized immobilization time, for the preparation of the apta-sensor.

The optimized apta-SARS-CoV-2-modified electrode (apta/AuNPs/CC) was then incubated with 1 μg/mL SARS-CoV-2 SP for 5, 15, 30, 45 and 60 min in PBS (pH 7.4) to establish the optimal time needed for the SP in solution to bind with the aptamer on the sensor surface. The occurrence of this process would result in a further current decrease due to the formation of the apta-SARS-CoV-2 SP complex, which causes the inhibition of both mass transport of the redox mediator towards the active electrode surface and the kinetic of the heterogeneous electron transfer process. In fact, as is shown in Figs. S5(c and d), the current density decreases with time up to 30 min, while it remains essentially constant for higher incubation times. Thus, 30 min was considered as the time needed for the formation of the apta-SARS-CoV-2 SP complex and afterward used for the construction of the calibration plots for the determination of the SP concentration.

The CV and DPV behaviors of the CC, AuNPs/CC, apta/AuNPs/CC and the SARS-CoV-2 SP bound to the apta/AuNPs/CC (SARS-CoV-2 SP/apta/AuNPs/CC) electrodes in the solution containing the $[Fe(CN)_6]^{3-/4-}$ redox probe are contrasted in Fig. 4a and b to highlight some important differences. Fig. 4a shows the effects on the CVs due to the various modifications made to the bare CC substrate. It is evident that, apart from the improvement of the electron transfer process after AuNPs deposition onto the surface of the CC (see discussion above), the immobilization of the aptamer and the subsequent formation of the complex with the SARS-CoV-2 SP led to the worsening of the overall electrode process. In fact, J_{pa} decreases (i.e., from about 2460 μA/cm^2 to about 857 μA/cm^2) and correspondingly the ΔE_p increases (i.e., from 0.088 to 0.388 V). These effects are similar to those reported in the literature, when bulky molecules (or other antibodies or aptamers) are immobilized onto an electrode surface (Hennessey et al., 2009; Mojsoska et al., 2021; Rahmati et al., 2021a,b). The DPVs (Fig. 4b) display a similar J_{pa} trend as above and, in addition, the shape of the voltammetric responses change from the well-defined peak, recorded at the AuNPs/CC, to those of flattened hills obtained at both apta/AuNPs/CC and SARS-CoV-2 SP/apta/AuNPs/CC electrodes. The above results are therefore congruent with an increasing hindering of both the heterogeneous electron transfer and mass transport towards the active zones of the electrode surface of the $[Fe(CN)_6]^{3-/4-}$ redox probe; the latter effect is mainly due to the interaction of SARS-CoV-2 SP with the immobilized aptamer layer, as also reported in other similar studies in the literature (Hennessey et al., 2009).

The AuNPs/CC surface modification with the aptamer and the subsequent binding of SP were also investigated by using CP, which has the advantage, over the electrochemical techniques that provide current/potential responses, of a constant ohmic drop effect, due to the constant current applied to the electrodes (Chowdhury et al., 2017). Fig. 4c shows the CP responses obtained at the AuNPs/CC, apta/AuNPs/CC, and SARS-CoV-2 SP/apta/AuNPs/CC (SP of 1 μg/mL) in the solution containing the $[Fe(CN)_6]^{3-/4-}$ redox couple. As is evident, the parameter τ from 34.4 s, recorded at the AuNPs/CC, increases to 105.5 s and 156.5 s for the apta/AuNPs/CC and SARS-CoV-2 SP/apta/AuNPs/CC electrodes, respectively. These results can be explained considering that, in the negative current step, the reduction of $[Fe(CN)_6]^{3-}$ occurs. Because the mass transport of the latter species towards the bulk medium is inhibited by the aptamer at the apta/AuNPs/CC and by the bulky SARS-CoV-2 SP at the SARS-CoV-2 SP/apta/AuNPs/CC, the active surface area is bathed by a larger concentration of the $[Fe(CN)_6]^{3-}$ and, consequently, at the applied constant current, the transition time τ of this step increases. These results suggest that at a given apta/AuNPs/CC, the lower the amount of SARS-CoV-2 SP, the lower the τ value.

The reproducibility of the preparation of the apta/AuNPs/CC was investigated by comparing the DPVs obtained in the solution containing

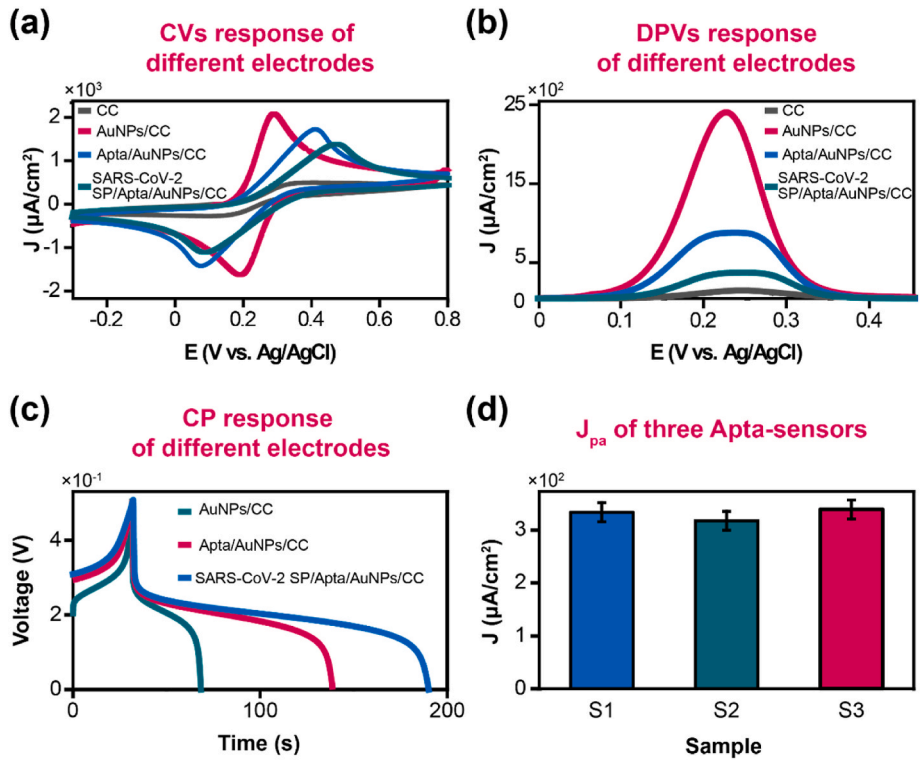

Fig. 4. (a,b,c) CV, DPV and CP responses, respectively, obtained at the various electrodes. (d) J_{pa} recorded by DPV at three different apta-sensors fabricated by using the optimized procedure and their responses after they were incubated in 1 μg/mL SARS-Cov-2 SP in PBS; it includes error bars, obtained from three replicates. All measurements were performed in the solution containing $[Fe(CN)_6]^{3-/4-}$ redox probe.

the $[Fe(CN)_6]^{3-/4-}$ redox probe, using three apta-sensors prepared under the above discussed optimized conditions, and after they were incubated with 1 μg/mL of SARS-CoV-2 SP (Fig. S6). The J_{pa} recorded at the three SARS-CoV-2 SP/apta/AuNPs/CC (Fig. 4d) provided an RSD of 1.52%.

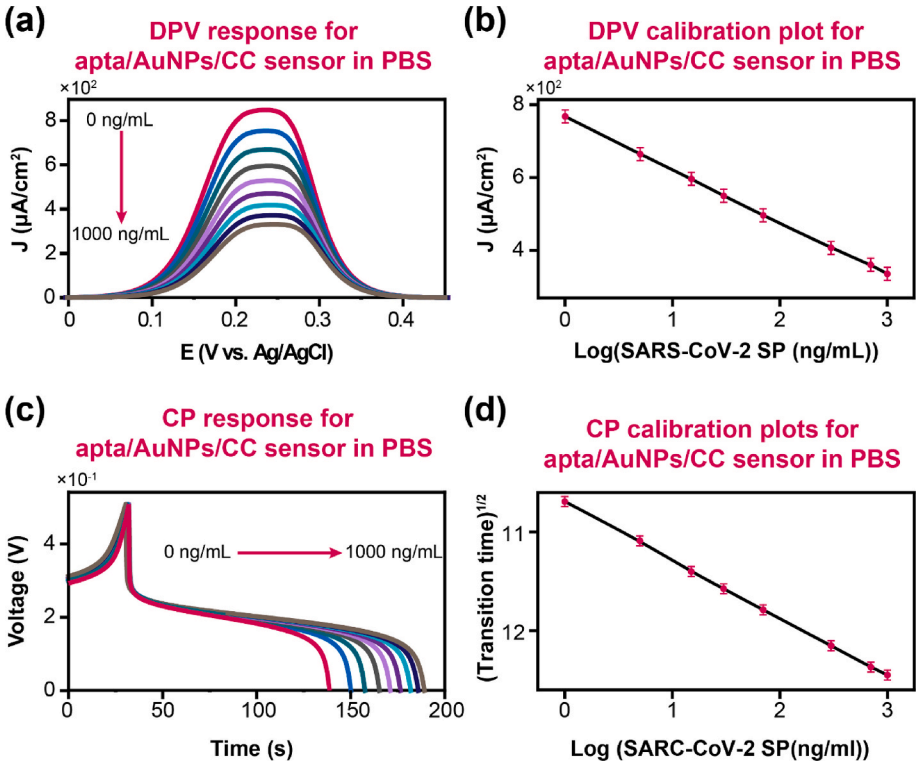

Fig. 5. (a,c) DPV and CP responses obtained at the apta/AuNPs/CC sensor incubated in PBS solutions containing different concentrations of SARS-CoV-2 SP (0, 2, 6, 20, 60, 200, 600, and 1000 ng/mL). (b,d) Calibration plots obtained using DPV and CP, respectively; they include error bars, obtained from three replicates. The star symbol refers to the responses obtained in the medium without SARS-CoV-2 SP. All measurements were performed in the solution containing $[Fe(CN)_6]^{3-/4-}$ redox probe.

3.4. Calibration plots and analytical performance

Calibration plots were obtained using the apta-sesnor incubated with different SARS-CoV-2 SP concentrations, and using both DPV and CP. The signals obtained at the apta/AuNPs/CC in the absence of SARS-CoV-2 SP were assumed as control. Therefore, J_{pa} or $\tau^{1/2}$ values, for the DPV and CP measurements, respectively, obtained in the absence and presence of SARS-CoV-2 SP were plotted against the logarithm of the SARS-CoV-2 SP concentration, as is typical for immunosensors (Adeel et al., 2022; Rahmati et al., 2021b; Yakoh et al., 2021). Fig. 5a,c shows a series of DPV and CP responses obtained at different SARS-CoV-2 SP concentrations in PBS. The J_{pa} and $\tau^{1/2}$ values in the absence of SARS-CoV-2 SP are indicated in the plots with different symbols. As is evident, using DPV J_{pa} decreases (Fig. 5b), while using CP $\tau^{1/2}$ increases (Fig. 5d), by increasing the SARS-CoV-2 SP concentration. In both cases linearity was observed (Fig. 5b,d), and the linear regression analysis of experimental points provided:

J_{pa} (μA/cm^2) = − (143.5 ± 1.1) log[SARS-CoV-2 SP] (ng/mL) + 764.9 (R^2 = 0.999) for DPV

$\tau^{1/2}$ ($s^{1/2}$) = − (0.589 ± 0.004) log[SARS-CoV-2 SP] (ng/mL) + 10.7 (R^2 = 0.999) for CP

Error bars included in the plots represent the standard deviation (Miller and Miller, 2005). The limit of detection (*LOD*) was obtained by the following relationship:

$$\mathrm{LOD} = 3\, S_N/m \quad (1)$$

where S_N is the standard deviation of J_{pa} or τ values (depending on the technique employed), obtained in the measurements performed with the sensor in the absence of SARS-CoV SP; m is the slope of the calibration plot. LODs thus evaluated were 0.11 ng/mL and 37.8 ng/mL using DPV and CP, respectively.

3.5. Application to real samples

The performance of the apta-sensor for the detection of SARS-CoV-2 SP was also examined in diluted human saliva (HS) samples. HS was diluted with PBS and subsequently spiked with different concentrations of SARS-CoV-2 SP. Fig. 6a,c shows the DPV and CP responses obtained for $[Fe(CN)_6]^{3-/4-}$ at the apta/AuNPs/CC sensor. As for the synthetic PBS solution, J_{pa} decreases and τ increases as SARS-CoV-2 SP increases. Plots of J_{pa} or $\tau^{1/2}$ against log[SARS-CoV-2 SP] are linear (Figs. S7b and d), and the linear regression analysis of experimental points provided the following equations:

J_{pa} (μA/cm^2) = − (154.91 ± 1.2) log[SARS-CoV-2 SP] (ng/mL) + 764.66 (R^2 = 0.999) for DPV

$\tau^{1/2}$ ($s^{1/2}$) = − (3.73 ± 1.47) log[SARS-CoV-2 SP] (ng/mL) + 10.76 (R^2 = 0.999) for CP

LODs, obtained by using equation (1) were of 0.17 ng/mL and 46.2 ng/mL for DPV and CP, respectively.

The analytical performances of the apta-sensor proposed here was compared with those obtained with other apta-sensors available in the literature for the detection of SARS-CoV-2 SP (Abrego-Martinez et al., 2022; Curti et al., 2022; Farrow et al., 2020; Jiang et al., 2021; Lasserre et al., 2022; Sari et al., 2022; Singh et al., 2021; Tabrizi et al., 2021; Tian et al., 2021; Zakashansky et al., 2021), and main analytical parameters are summarized in Table S1. As is evident, the use of DPV provided a LOD which is better or comparable with those reported in the literature for other similar aptasensors. LOD obtained by CP, although higher than that of DPV, is still better than those obtained with other Au-coated electrode systems (Table S1).

3.6. Selectivity, repeatability, and stability of the sensor

The selectivity was examined by comparing the DPV current density responses for the $[Fe(CN)_6]^{3-/4-}$ redox probe obtained with the apta/AuNPs/CC sensor in solutions containing SARS-CoV-2 SP (1 μg/mL), SARS-CoV SP (5 μg/mL), BSA (5 μg/mL) and HSA (5 μg/mL). J_{pa} values obtained are shown, as histograms, in Fig. 6a, and the corresponding DPVs are shown in Fig. S8. As is evident, in the presence of SARS-CoV-2 SP, J_{pa} decreases, as expected, to a considerable extent. Instead, in the

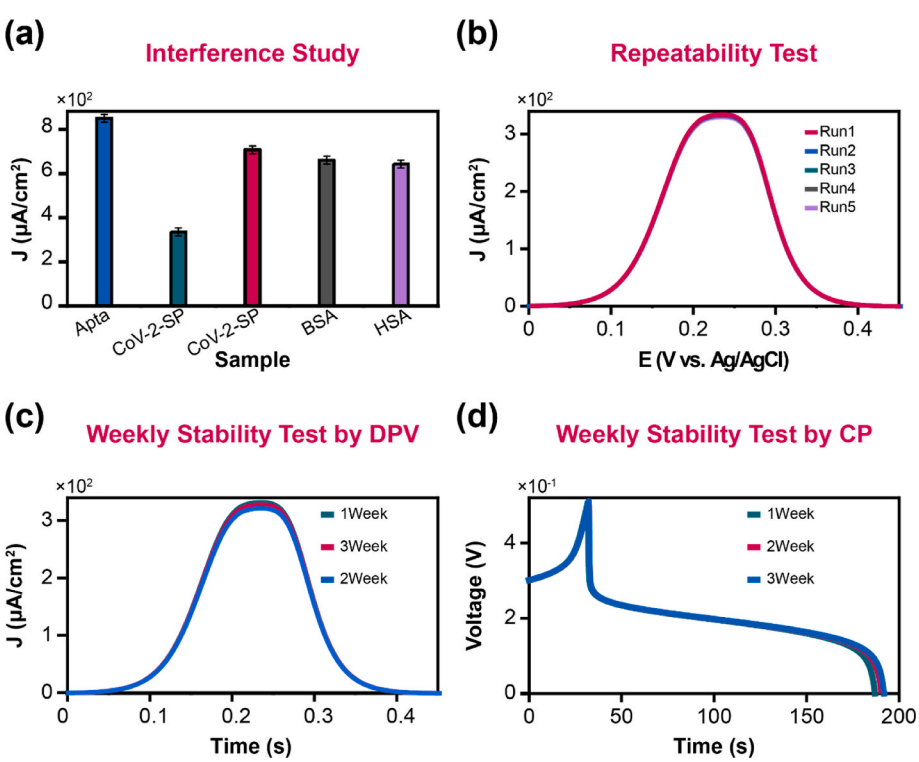

Fig. 6. (a) Histograms of the current densities obtained at the apta/AuNPs/CC sensor incubated in PBS solutions containing SARS-CoV SP (5 μg/mL), SARS-CoV-2 SP (1 μg/mL), BSA (5 μg/mL) and HSA (5 μg/mL); (b) five DPVs obtained at apta/AuNPs/CC after incubation with 1 μg/mL SARS-CoV-2 SP; (c–d) DPVs and CPs of a freshly prepared apta/AuNPs/CC sensor, after it had been stored up to 3 weeks at 4 °C (measurements were performed at a week interval) and incubated in 1 μg/mL SARS-CoV-2 SP in PBS. All measurements were performed in the solution containing $[Fe(CN)_6]^{3-/4-}$ redox probe.

presence of SARS-CoV SP, BSA and HAS, J_{pa} decreased to a much lower extent indicating that the apta-sensor proposed here is highly specific to SARS-CoV-2 SP.

The reusability of the apta-sensor was investigated during 3 weeks at a weak interval, storing the sensor at 4 °C until use. The J_{pa} of $[Fe(CN)_6]^{3-/4-}$ redox probe, recorded by DPV after binding SARS-CoV-2 SP (1 μg/mL in PBS) provided RSD of 2.42% from five replicates (Fig. 6c). Also, similar results were obtained by CP measurements, where a lower RSD value of 1.8% was obtained (Fig. 6d).

4. Conclusions

In this work, AuNPs-coated carbon cloth electrodes, modified with a thiol functionalized DNA aptamer were prepared and used for the label-free detection of SARS-CoV-2 SP. The analytical responses were obtained by using the electrochemical techniques DPV and CP. The study showed that both techniques provided good analytical performances, which in terms of LODs were of 0.11 ng/mL and 0.38 ng/mL using DPV and CP, respectively, in PBS solutions, and correspondingly of 0.17 ng/mL and 46.2 ng/mL in diluted human saliva samples. In addition, the purposed apta-sensor could be re-used for at least three weeks with negligible changes in the analytical performance. Interference due to SARS-CoV, BSA and HSA was minimal, while repeatability of the responses was very good. The incubation time required for the SARS-CoV-2 SP to produce the suitable electrochemical signals was short. All these characteristics are better or comparable with those of other aptasensors reported in the literature, and in general are adequate for practical clinical applications.

Because one of the mayor mechanisms of COVID-19 spread is through aerosol droplets expelled from infected persons, detection of SARS-CoV-2 SP in exhaled breath condensate might represent an important alternative specimen for diagnosing the COVID-19 disease. Since the carbon-based material employed for the construction of the proposed sensor is highly flexible and did not lose the mechanical stability when bent on various angles, it can be adapted to non-flat surfaces, such as face masks, where breath condensate can be collected and examined by the methods described here. However, a proper optimization of the device, along with miniaturized electronics for data transmission, are necessary before making a prototype device. Studies in this direction have been planned in our laboratories.

CRediT authorship contribution statement

Muhammad Adeel: and. **Kanwal Asif:** Conceptualization, Writing – original draft. **Fahad Alshabouna:** and. **Vincenzo Canzonieri:** Writing – review & editing, Funding acquisition. **Md Mahbubur Rahman:** and. **Sajid Ali Ansari:** Formal analysis, Writing – review & editing. **Firat Güder:** Writing – review & editing. **Flavio Rizzolio:** and. **Salvatore Daniele:** Conceptualization, Formal analysis, Writing – review & editing.

Declaration of competing interest

The authors declare that they have no known competing financial interests or personal relationships that could have appeared to influence the work reported in this paper.

Data availability

Data will be made available on request.

Acknowledgment

This work was with the COST Action STRATAGEM CA17104, supported by COST (European Cooperation in Science and Technology) (www.cost.eu), and also within the program SPIN-Supporting Principal Investigators, Ca' Foscari University Venice, Italy, N° 9L2AC3B8.

Appendix A. Supplementary data

Supplementary data to this article can be found online at https://doi.org/10.1016/j.biosx.2022.100256.

References

Abrego-Martinez, J.C., Jafari, M., Chergui, S., Pavel, C., Che, D., Siaj, M., 2022. Biosens. Bioelectron. 195, 113595.
Adeel, M., Asif, K., Canzonieri, V., Barai, H.R., Rahman, M.M., Daniele, S., Rizzolio, F., 2022. Sensor. Actuator. B Chem. 359, 131591.
Adeel, M., Canzonieri, V., Daniele, S., Rizzolio, F., Rahman, M.M., 2021a. J. Ind. Eng. Chem. 103, 165–174.
Adeel, M., Canzonieri, V., Daniele, S., Vomiero, A., Rizzolio, F., Rahman, M.M., 2021b. Microchim. Acta 188.
Adeel, M., Rahman, M.M., Caligiuri, I., Canzonieri, V., Rizzolio, F., Daniele, S., 2020. Biosens. Bioelectron. 165, 112331.
Adeel, M., Rahman, M.M., Lee, J.J., 2019. Biosens. Bioelectron. 126, 143–150.
Amatore, C., Savéant, J.M., Tessier, D., 1983. J. Electroanal. Chem. 147, 39–51.
Bai, L., Elósegui, C.G., Li, W., Yu, P., Fei, J., Mao, L., 2019. Front. Chem. 7, 313.
Bard, A.J., Faulkner, L.R., 2001. Electrochemical Methods: Fundamental and Applications, second ed. Wiley.
Beduk, T., Beduk, D., de Oliveira Filho, J.I., Zihnioglu, F., Cicek, C., Sertoz, R., Arda, B., Goksel, T., Turhan, K., Salama, K.N., Timur, S., 2021. Anal. Chem. 93, 8585–8594.
Chaibun, T., Puenpa, J., Ngamdee, T., Boonapatcharoen, N., Athamanolap, P., O'Mullane, A.P., Vongpunsawad, S., Poovorawan, Y., Lee, S.Y., Lertanantawong, B., 2021. Nat. Commun. 12, 802.
Cho, I.H., Kim, D.H., Park, S., 2020. Biomater. Res. 24, 1–12.
Chowdhury, N.R., Kumar, R., Kant, R., 2017. J. Electroanal. Chem. 802, 64–77.
Coronavirus Disease, 2019. COVID-19) Emergency Use Authorizations for Medical Devices. FDA, 2020.
Curti, F., Fortunati, S., Knoll, W., Giannetto, M., Corradini, R., Bertucci, A., Careri, M., n, d., 2022. ACS Appl. Mater. Interfaces 14 (17), 19204–19211.
Da Ruos, J., Baldo, M.A., Daniele, S., 2022. Da Ruos et al. 2022. Crit. Rev. Anal. Chem. 1–35, 2039094.
El Keshky, M.E.S., Basyouni, S.S., Al Sabban, A.M., 2020. Front. Psychol. 11, 585897.
Farrow, T., Laumier, S., Sandall, I., Zalinge, H. Van, 2020. Res. Square 17, 1–10.
Hachim, A., Kavian, N., Cohen, C.A., Chin, A.W.H., Chu, D.K.W., Mok, C.K.P., Tsang, O.T.Y., Yeung, Y.C., Perera, R.A.P.M., Poon, L.L.M., Peiris, J.S.M., Valkenburg, S.A., 2020. Nat. Immunol. 21, 1293–1301.
Hennessey, H., Afara, N., Omanovic, S., Padjen, A.L., 2009. Anal. Chim. Acta 643, 45–53.
Hopkins, J., Fidanovski, K., Lauto, A., Mawad, D., 2019. Front. Bioeng. Biotechnol. 7, 237.
Jiang, C., Mu, X., Du, B., Tong, Z., 2022. Micro & Nano Lett. 17, 49–58.
Jiang, Z.W., Zhao, T.T., Li, C.M., Li, Y.F., Huang, C.Z., 2021. ACS Appl. Mater. Interfaces 13, 49754–49761.
Jo, H., Gu, H., Jeon, W., Youn, H., Her, J., Kim, S.K., Lee, J., Shin, J.H., Ban, C., 2015. Anal. Chem. 87, 9869–9875.
Kevadiya, B.D., Machhi, J., Herskovitz, J., Oleynikov, M.D., Blomberg, W.R., Bajwa, N., Soni, D., Das, S., Hasan, M., Patel, M., Senan, A.M., Gorantla, S., McMillan, J.E., Edagwa, B., Eisenberg, R., Gurumurthy, C.B., Reid, S.P.M., Punyadeera, C., Chang, L., Gendelman, H.E., 2021. Nat. Mater. 20, 593–605.
Khan, M.E., 2021. Nanoscale Adv. 3, 1887–1900.
Kour, R., Arya, S., Young, S.-J., Gupta, V., Bandhoria, P., Khosla, A., 2020. J. Electrochem. Soc. 167, 037555.
Kumar, N., Shetti, N.P., Jagannath, S., Aminabhavi, T.M., 2022. Chem. Eng. 430, 1385–8947.
Lai, C.C., Wang, C.Y., Ko, W.C., Hsueh, P.R., 2021. J. Microbiol. Immunol. Infect. 54, 164–174.
Lasserre, P., Balansethupathy, B., Vezza, V.J., Butterworth, A., Macdonald, A., Blair, E.O., McAteer, L., Hannah, S., Ward, A.C., Hoskisson, P.A., Longmuir, A., Setford, S., Farmer, E.C.W., Murphy, M.E., Flynn, H., Corrigan, D.K., 2022. Anal. Chem. 94, 2126–2133.
Lim, S.A., Ahmed, M.U., 2016. RSC Adv. 6, 24995–25014.
Lopa, N.S., Rahman, M.M., Ahmed, F., Ryu, T., Sutradhar, S.C., Lei, J., Kim, J., Kim, D.H., Lee, Y.H., Kim, W., 2019. Biosens. Bioelectron. 126, 381–388.
H. Lu, B. He, B. Gao, 2021, 2, ER, 175-181.
Lukose, J., Chidangil, S., George, S.D., 2021. Biosens. Bioelectron. 178, 113004.
Maduraiveeran, G., Jin, W., 2017. Trends Environ. Anal. Chem 13, 10–23.
Maehashi, K., Katsura, T., Kerman, K., Takamura, Y., Matsumoto, K., Tamiya, E., 2007. Anal. Chem. 79, 782–787.
Medley, C.D., Smith, J.E., Tang, Z., Wu, Y., Bamrungsap, S., Tan, W., 2008. Anal. Chem. 80, 1067–1072.
Miller, J., Miller, J., 2005. Staitistics and Chemometrics for Analytical Chemistry, fifth ed. Pearson Education Limited, Harlow.
Min, K., Cho, M., Han, S.Y., Shim, Y.B., Ku, J., Ban, C., 2008. Biosens. Bioelectron. 23, 1819–1824.
Mojsoska, B., Larsen, S., Olsen, D.A., Madsen, J.S., Brandslund, I., Alatraktchi, F.A., 2021. Sensors 21, 390.
Pirzada, M., Altintas, Z., 2019. Sensors 19 (23), 5311.
Rahman, M.M., 2022. Chemosensors 10, 287.

Rahmati, Z., Roushani, M., Hosseini, H., Choobin, H., 2021a. Microchim. Acta 188, 105.
Rahmati, Z., Roushani, M., Hosseini, H., Choobin, H., 2021b. Microchem. J. 170, 106718.
Raziq, A., Kidakova, A., Boroznjak, R., Reut, J., Öpik, A., Syritski, V., 2021. Biosens. Bioelectron. 178, 113029.
Sari, K.A., Yeni Wahyuni, Hartati, Gaffar, Shabarni, Isa, Anshori, Hidayat, Darmawan, Wiraswati, Hesti Lina, 2022. J. Electrochem. Sci. Eng. 12, 219–235.
Seo, G., Lee, G., Kim, M.J., Baek, S.H., Choi, M., Ku, K.B., Lee, C.S., Jun, S., Park, D., Kim, H.G., Kim, S.J., Lee, J.O., Kim, B.T., Park, E.C., Kim, S. Il, 2020. ACS Nano 14, 5135–5142.
Singh, N.K., Ray, P., Carlin, A.F., Magallanes, C., Morgan, S.C., Laurent, L.C., Aronoff-Spencer, E.S., Hall, D.A., 2021. Biosens. Bioelectron. 180, 113111.
Stanborough, T., Given, F.M., Koch, B., Sheen, C.R., Stowers-Hull, A.B., Waterland, M.R., Crittenden, D.L., 2021. ACS Omega 6 (9), 6404–6413.
Tabrizi, A.M., Nazari, L., Acedo, P., 2021. Sensor. Actuator. B Chem. 345, 130377.
Taleghani, N., Taghipour, F., 2021. Biosens. Bioelectron. 167, 112478.
Tian, J., Liang, Z., Hu, O., He, Q., Sun, D., Chen, Z., 2021. Electrochim. Acta 387, 138553.
Wang, C., Horby, P.W., Hayden, F.G., Gao, G.F., 2020. Lancet 395, 470–473.
Wouters, O.J., Shadlen, K.C., Salcher-Konrad, M., Pollard, A.J., Larson, H.J., Teerawattananon, Y., Jit, M., 2021. Lancet 397, 1023–1034.
Yakoh, A., Pimpitak, U., Rengpipat, S., Hirankarn, N., Chailapakul, O., Chaiyo, S., 2021. Biosens. Bioelectron. 176, 112912.
Ying, L., Yue-Ping, L., Bo, D., Feifei, R., Yue, W., Jinya, D., Qianchuan, H., 2020. medRxiv 26, 20044883.
Yüce, M., Filiztekin, E., Özkaya, K.G., 2021. Biosens. Bioelectron. 172, 956–5663.
Zakashansky, J.A., Imamura, A.H., Salgado, D.F., Romero Mercieca, H.C., Aguas, R.F.L., Lao, A.M., Pariser, J., Arroyo-Currás, N., Khine, M., 2021. Anal. Methods 13, 874–883.
Zhang, J., Xia, Z., Dai, L., 2015. Sci. Adv. 1, e1500564.
Zhao, H., Liu, F., Xie, W., Zhou, T.C., OuYang, J., Jin, L., Li, H., Zhao, C.Y., Zhang, L., Wei, J., Zhang, Y.P., Li, C.P., 2021. Sensor. Actuator. B Chem. 327, 128899.